ADVANCED MATERIALS TECHNOLOGIES
www.advmattechnol.de

Rationally Engineered Vertically Aligned β-$Ga_{2-x}W_xO_3$ Nanocomposites for Self-Biased Solar-Blind Ultraviolet Photodetectors with Ultrafast Response

*Debabrata Das, Francelia Sanchez, Dallin J. Barton, Susheng Tan, Vaithiyalingam Shutthanandan, Arun Devaraj, and Chintalapalle V. Ramana**

With the astonishing advancement of present technology and increasing energy consumption, there is an ever-increasing demand for energy-efficient multifunctional sensors or transducers based on low-cost, eco-friendly material systems. In this context, self-assembled vertically aligned β-$Ga_{2-x}W_xO_3$ nanocomposite (GWO-VAN) architecture-assisted self-biased solar-blind UV photodetection on a silicon platform, which is the heart of traditional electronics is presented. Utilizing precisely controlled growth parameters, the formation of W-enriched vertical β-$Ga_{2-x}W_xO_3$ nanocolumns embedded into the W-deficient β-$Ga_{2-x}W_xO_3$ matrix is reached. Detailed structural and morphological analyses evidently confirm the presence of β-$Ga_{2-x}W_xO_3$ nanocomposite with a high structural and chemical quality. Furthermore, absorption and photoluminescence spectroscopy explains photo-absorption dynamics and the recombination through possible donor–acceptor energy states. The proposed GWO-VAN framework facilitates evenly dispersed nanoregions with asymmetric donor energy state distribution and thus forms build-in potential at the vertical β-$Ga_{2-x}W_xO_3$ interfaces. As a result, the overall heterostructure evinces photovoltaic nature under the UV irradiation. A responsivity of ≈30 A/W is observed with an ultrafast response time (≈350 µs) under transient triggering conditions. Corresponding detectivity and external quantum efficiency are 7.9×10^{12} Jones and 1.4×10^4%, respectively. It is believed that, while this is the first report exploiting GWO-VAN architecture to manifest self-biased solar-blind UV photodetection, the implication of the approach is enormous in designing electronics for extreme environment functionality and has immense potential to demonstrate drastic improvement in low-cost UV photodetector technology.

1. Introduction

The discovery, design, and development (3-D) of novel materials with superiority (enhanced performance), scalability, and survivability (3-S) under extreme conditions of operation is most critical to enable advancements in many of the current and next-generation technologies. This strategy is critically and specifically important to all those emerging technologies which are at the interface of multidisciplinary fields such as energy, environment, and space, national security, and biomedicine. Solar-blind ultraviolet (UV) photodetector (PD) technology is one among them. Since the introduction of modern nanotechnology, solar-blind UV-PD has drawn a tremendous recent interest due to its multifunctional applicability in various intense technological research fields, such as biomedical imaging, weather monitoring, missile tracking, ozone monitoring, flame sensing, dip ultraviolet photonic applications, etc.[1–4] In particular, an immense effort to realize advanced communication systems has brought a new concept, the "Internet of Things."It has exaggerated the 3D research on low cost, high sensitivity, fast response, environment-friendly,

D. Das, F. Sanchez, C. V. Ramana
Center for Advanced Materials Research (CMR)
University of Texas at El Paso
500 W University Ave, El Paso, TX 79968, USA
E-mail: rvchintalapalle@utep.edu

D. Das, C. V. Ramana
Department of Aerospace and Mechanical Engineering
University of Texas at El Paso
500 W University Ave, El Paso, TX 79968, USA

F. Sanchez
Department of Metallurgical
Materials, and Biomaterials Engineering
University of Texas at El Paso
500 W University Ave, El Paso, TX 79968, USA

D. J. Barton, V. Shutthanandan, A. Devaraj
Environmental Molecular Sciences Laboratory (EMSL)
Pacific Northwest National Laboratory (PNNL)
Richland, WA 99352, USA

S. Tan
Department of Electrical and Computer Engineering and Petersen
Institute of NanoScience and Engineering
University of Pittsburg
Pittsburgh, PA 15261, USA

The ORCID identification number(s) for the author(s) of this article can be found under https://doi.org/10.1002/admt.202300014

DOI: 10.1002/admt.202300014

durable, energy-efficient, and multifunctional sensing devices on the same platform. Recently, the scientific, engineering, and technology development community explored various wide and ultrawide bandgap material systems, such as gallium nitride, aluminum gallium nitride, zinc oxide, magnesium zinc oxide, titanium oxide, germanium oxide, nickel oxide, tin oxide, and so on, where the focus was 3-S criteria.[3,5–10] Undoubtedly, recent efforts have demonstrated various material synthesis and fabrication processes in addition to novel device architectures. However, there exist many fundamental, technical drawbacks in those aforementioned specific approaches, which are not ideal in the context of multi-functionality and the success and longevity of emerging technologies. For instance, to illustrate the scientific challenges, the growth of defect-free nitride semiconductors is very challenging and needs a higher thermal budget.[3,11,12] Simultaneously, incorporating aluminum to push the optical window toward deep UV creates clustering and percolation effects.[13] Thus, it reduces the overall device performance. Also, the growth of complex stoichiometric oxides is exceptionally challenging. Therefore, the search and 3-D aspects of research activities must be continued while considering the rationally designed or engineered novel architectures based on advanced concepts in order to find exceptionally high-performance materials with 3-S criteria.

Gallium oxide (Ga_2O_3), an ultrawide band gap material, has exciting potential for integration into next-generation electronic, optoelectronic, photonic, and sensing devices because of its favorable intrinsic properties.[14–20] Ga_2O_3 exhibits polymorphism consisting of six crystalline phases α, β, γ, δ, ϵ, and κ.[14,17,18,21] Monoclinic β-Ga_2O_3 has been researched the most as it possesses chemical and thermal stability from room temperature to its melting point. All the other phases are considered as metastable states and transform into monoclinic phase upon heat treatment. β-Ga_2O_3 has a large band gap of 4.9–5.0 eV, an estimated breakdown field of 8 MV cm^{-1}, and a melting point of approximately 1800 °C.[14–16,18] Because of its thermal stability, β-Ga_2O_3 can be grown from the melt, reducing fabrication costs.[18] Additionally, β-Ga_2O_3 presents fascinating optical properties, including transparency in near UV, visible, and near-infrared spectral regions with no absorption.[14–16] As with any other emerging material, basic properties must be understood and controlled to exploit their highest potential. Therefore, doping and alloying aspects of β-Ga_2O_3 were investigated to improve the conductivity and tailoring of the optical band gap. Some of the dopants include Si, Sn, B, Fe, and Ge.[17,18] β-Ga_2O_3 has been alloyed with Al_2O_3, In_2O_3, and N to tailor its band gap, carrier mobility, and thermal conductivity.[14,18] For instance, previously, we have explored the effects of Sn doping in β-Ga_2O_3 to improve its electrocatalysis and electrochemical energy storage capability.[17,22] Because of its versatile properties, β-Ga_2O_3 has found multitudinous applications, such as field effect transistors, solar-blind ultraviolet detectors, solar cells, gas sensors, catalysts, photocatalysts, deep UV PDs, diodes, X-ray detectors, and phototransistors.[4,18] In this contribution, for the first time, we demonstrate the high-performance, self-biased solar-blind ultraviolet photodetectors based on rationally engineered W-incorporated β-Ga_2O_3 (GWO) nanocomposites. The goal is to realize such high-performance and self-biased photodetectors onto silicon, which is well studied and highly integrated substrate material platform into nanoelectronics and nanophotonics, and eliminate the expensive and highly sophisticated choices in terms of processing and substrate materials.

As the emphasis in this work is toward the multifunctional applicability of nanocomposites made from high band gap β-Ga_2O_3, it is worthwhile to discuss about nanocomposite (NC) thin films.[23] With the increasing demand for multifunctional devices on the same platform, the NC synthesis strategy has become extremely popular. In situ or ex situ integration of a secondary phase inside the host matrix or evenly distributed multiple phases in a nanometer scale dimension have shown superior performance. Though the concept of NC was introduced into the literature long ago, researchers have started using this concept dedicatedly in recent years. Self-assembled or templated NC have gained enormous attention because of their massive span of multidimensional applicability.[23–29] Noteworthy, ferromagnetic, ferroelectric, piezocapacitive, multiferroic, photovoltaic, plasmonic, optical nonlinearity, semiconducting, superconducting, solid electrolyte, and data storage are a few among many other potential applications.[23,24,30–33] The fabrication of such NCs can be classified into two main categories.[23] The top–down is the first and includes nanoimprinting, colloidal lithography, electron beam lithography, and focused ion beam lithography. The second approach is the bottom–up approach which exploits the in situ self-assembly of nano-textured composites. In addition, template-assisted growth and electrochemical anodization are essential to mention. Mainly, three different NC configurations exist in the literature: particle-in-matrix, multilayer superlattice, and vertically aligned NC (VAN).[23,32]

In the present work, we focused on designing the self-biased, self-powered solar-blind UV photodetectors based on Ga-oxide nanocomposites. There are several reports in the existing literature that combine photodetection and NC technology. For example, Guo et al.[34] demonstrated ZnO-polymer NC PD showing specific detectivity of 3.4×10^{15} Jones by utilizing interfacial trap states as an effective medium for enhanced charge injection. Similarly, numerous attempts exist to exploit conductive polymer and high band gap metal oxide NC to improve the PD figure of merit.[35,36] Jin et at.[37] have gone one step forward and have prepared graphdiyne- ZnO NC for high-performance UV PD. However, to the best of our knowledge, scientists have utilized mainly the particle-in-matrix approach in NC regime to manifest novel UV PD architecture. While efforts directed in that direction have achieved and/or shown significant improvement in PD figure of merits, but hardly any reports facilitating the concept of photovoltaic self-powered photodetection. Here, we propose and demonstrate an approach to accomplish this using GWO-VAN nanocomposites.

Under the enlightenment of the aforementioned discussion of nanocomposites-based UV-PDs, we propose a new approach to realize cost-effective, self-powered solar-blind UV PD by exploiting the VAN technique.[23] It is already proven that pulsed laser deposition (PLD) can utilize preferential crystal orientation, self-assembly, interfacial phase stabilization, and parallel nucleation of multiple phases to demonstrate various exotic NC thin films.[38] For instance, horizontal-vertical-diagonal superlattice, nanodots in host matrix, and vertically aligned multiphase nanocolumns are some of the important

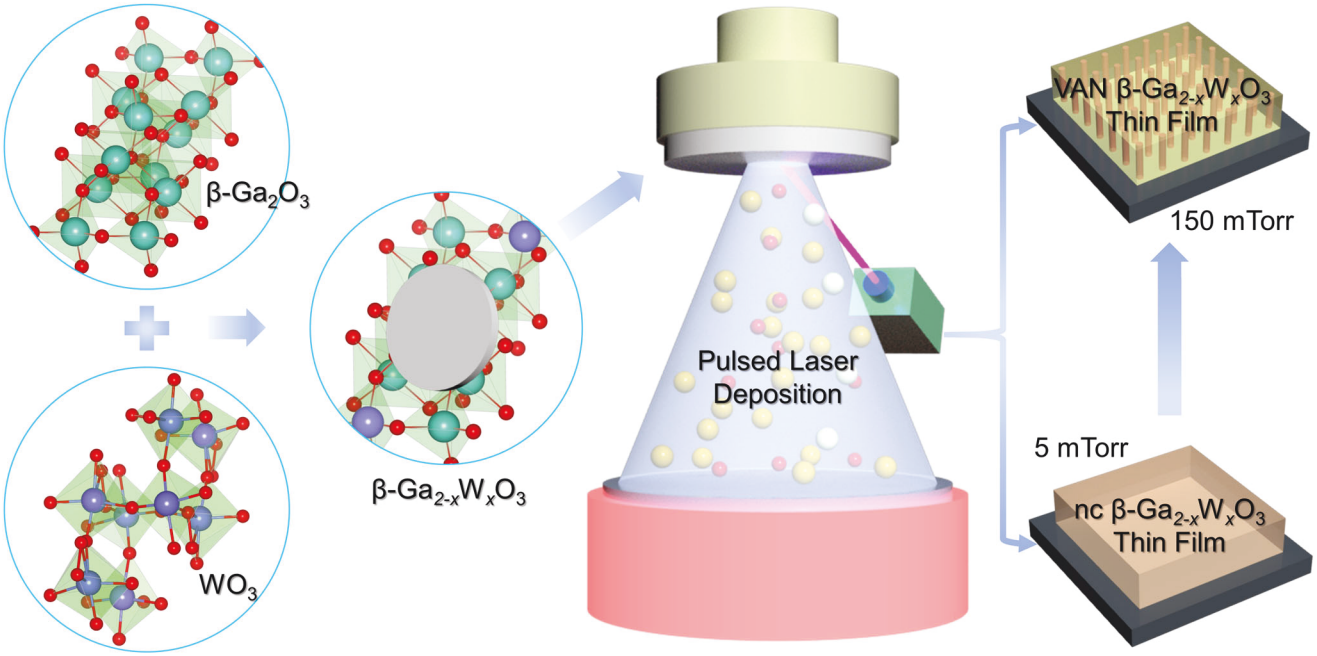

Figure 1. Schematic of the overall fabrication process, starting with pure β-Ga_2O_3 and WO_3 powder to β-$Ga_{2-x}W_xO_3$ target preparation and, last, tailoring of nanocrystalline (nc) β-$Ga_{2-x}W_xO_3$ thin film into VAN architecture by pressure controlled PLD.

nanotextured films viable in PLD technique under controlled tuning of in-situ parameters.[23,38] Moreover, we have already demonstrated high-quality PLD-grown nano-textured β-Ga_2O_3 thin films on Si substrate, where controlled parameters facilitate nucleation of selective crystal orientations and growth of close compact nanocolumnar β-Ga_2O_3 thin film.[21] The high pressure-high temperature structure-zone growth mode and asymmetric thermal conductivity provided self-assembled nanocolumnar β-Ga_2O_3 with fantastic structural and optical properties.[21]

Our approach (see, **Figure 1**) is to utilize rationally engineered GWO materials in design of the high-performance solar-blind UV photodetectors. Here, we have successfully tailored the W incorporated β-Ga_2O_3 in the form of highly textured β-$Ga_{2-x}W_xO_3$ VAN using controlled in situ O_2 partial pressure (pO_2). Figure 1 shows the schematic of the overall fabrication process, where engineering GWO-VAN is demonstrated starting from pure β-Ga_2O_3 and WO_3 powders to VAN thin film on Si substrate. Both β-Ga_2O_3 and WO_3 show stable monoclinic crystal structures but require different growth conditions to be stabilized in the nanocrystalline phase. Due to the variation in formation energy and surface diffusion rate, pO_2 can easily control the W incorporation probability into the final matrix. Moreover, the perfectly tuned PLD process can stabilize it in a close compact nanocolumnar phase. Optimizing growth conditions allowed us to engineer and stabilize the W-enriched nanocolumnar β-$Ga_{2-x}W_xO_3$ architecture inside the W-deficit β-$Ga_{2-x}W_xO_3$ matrix. As a result, there exist evenly distributed nanoregions with asymmetric donor energy levels, which facilitate the self-powered separation of photogenerated charge carriers and, thus, solar-blind photovoltaic UV PD. We believe this innovative VAN approach to demonstrate low-cost self-biased deep UV photodetection can be the road map for futuristic PDs in a wide range of technological applications.

2. Results and Discussion

The X-ray diffraction (XRD) patterns of β-$Ga_{2-x}W_xO_3$ NCs, with varying O_2 partial pressure, are illustrated in **Figure 2**a. Corresponding peaks are in good agreement with β-Ga_2O_3 powder diffraction patterns (JCPDS Card No. 00-041-1103).[39] Though the target used for PLD deposition contains W, no diffraction peaks due to WO_3 were observed after sintering the PLD target. Similarly, we have not seen any sign of the WO_3 phase in as-grown β-$Ga_{2-x}W_xO_3$ films. Only exists relative broadening and asymmetric nature of the corresponding diffraction peaks related to β-Ga_2O_3. The initial evidence points toward phase pure ternary β-$Ga_{2-x}W_xO_3$ nanocrystalline thin film stabilization on Si/SiO_2 interface. We believe that the phase pure β-$Ga_{2-x}W_xO_3$ NC films are due to a combination of factors. Specifically, we believe that the strategy of W incorporation into β-Ga_2O_3 matrix during the pulsed laser-assisted growth fulfills the Hume–Rothery rules. The requirements are satisfied because the ionic radii of Ga^{3+} and W^{6+} differ less than 15% (the ionic radius of Ga^{3+} and W^{6+} is 0.062 and 0.060 nm, respectively) and both β-Ga_2O_3 and WO_3 oxides stabilize in monoclinic phase at room temperature. Additionally, the electronegativity of Ga is similar to W atoms (1.6 and 1.7 Pau for Ga and W, respectively). Relatively low pO_2 (5–50 mTorr) reflects lower intensity diffraction peaks of selective lattice orientations, such as $(\bar{2}01)$, $(\bar{4}02)$, $(\bar{6}03)$, $(\bar{4}01)$, $(\bar{6}01)$, and $(\bar{8}01)$. Similar texturing was reported earlier in pulsed laser-deposited pure β-Ga_2O_3 thin films on Si substrate.[21] With increasing pO_2, the overall peak intensity increases and gradually introduces additional crystal planes, including (400) and (600). Figures S1a,b, Supporting Information, show relative tailoring of (400) and $(\bar{4}01)$ peaks and corresponding peak intensity ratios with increasing pO_2, respectively. They show a gradual dominating of (400) peak at higher O_2 concentrations. Moreover, the peak corresponding to $(\bar{8}01)$ become more prominent in

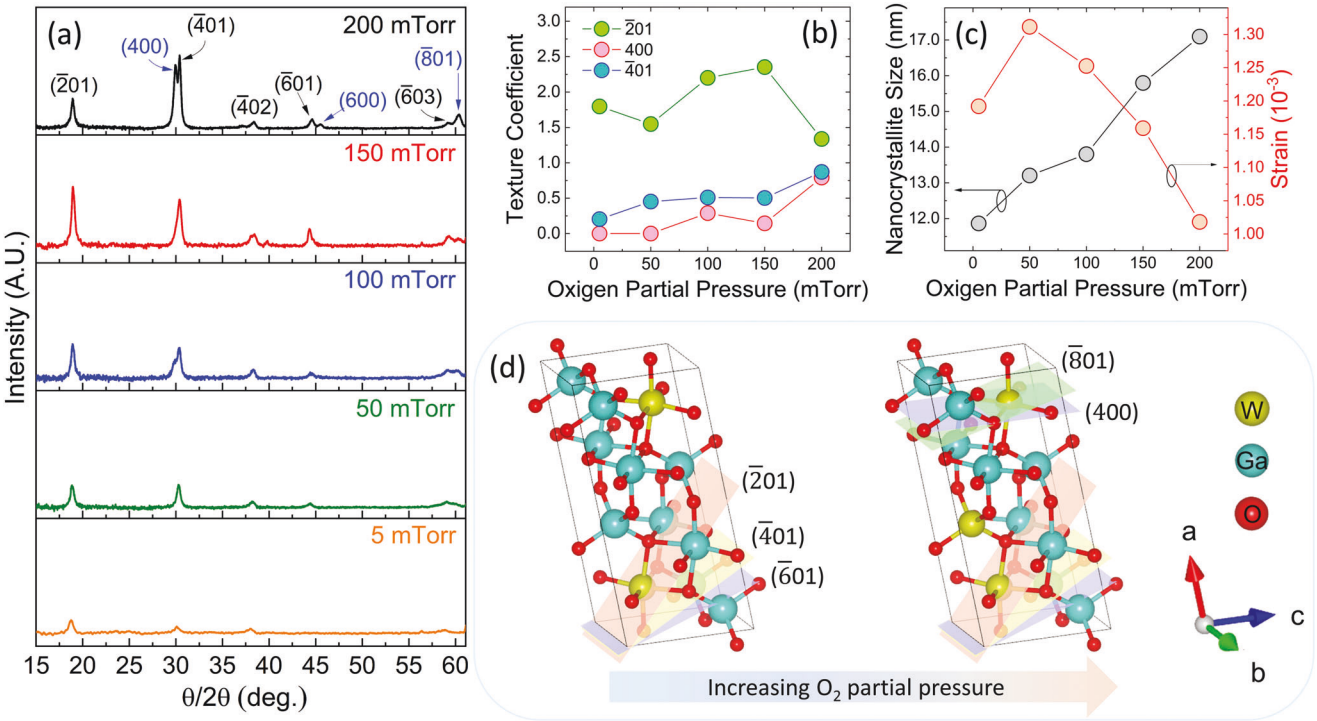

Figure 2. a) High-resolution X-ray diffraction patterns with increasing O_2 partial pressure; b) Texture coefficient of selected crystal orientations ($(\bar{2}01)$, (400), and $(\bar{4}01)$); c) O_2 partial pressure dependent variation of nanocrystallite size and strain; d) Schematic of β-$Ga_{2-x}W_xO_3$ crystal structure showing increasing W incorporation induced tailoring of preferred crystal orientation.

comparison with $(\bar{6}03)$ at the highest pO_2. Figure 2d portrays a schematic of how the preferred crystal orientation evolves with increasing pO_2. It is apparent from the relative intensity of the diffraction peaks that crystallinity improves with increasing pO_2. For further analysis, we have investigated the progression of nanocrystallite size, strain, and texture coefficient of dominated crystal orientations (Figure 2b,c). The crystallite size (D) was calculated using the Scherrer equation

$$D = \frac{K\lambda}{\beta\cos\theta} \tag{1}$$

where K is the shape factor in the range 0.8 −1.2 ($K = 0.9$), λ is the X-ray wavelength of Cu Kα = 1.5406 Å, β is the FWHM value, and θ is the diffraction angle. Additionally, the peaks tend to shift toward higher angles as the pO_2 increases. The lattice strain (ϵ) is calculated using the following equation:

$$\epsilon = \frac{\beta}{4}\tan\theta \tag{2}$$

Last, the texture coefficient (TC) is estimated using the following equation:

$$TC = \frac{N\left(\frac{I_{(hkl)}}{I_{o(hkl)}}\right)}{\sum_n\left(\frac{I_{(hkl)}}{I_{o(hkl)}}\right)} \tag{3}$$

Here, N is the total number of reflections, n is the number of diffraction peaks, $I_{(hkl)}$ is the intensity calculated from experimental data for a (hkl) the specified plane, and $I_{o_{(hkl)}}$ is the standard intensity obtained from the JCPDS cards corresponding to the same (hkl) planes. The plane with the highest TC is $(\bar{2}01)$, followed by $(\bar{4}01)$ and (400) planes, where TC of $(\bar{2}01)$ plane reaches its maximum at pO_2 = 150 mTorr (Figure 2b). The rest show an overall increment in TC with higher pO_2. Also, nanocrystallite size shows a similar trend (Figure 2c), whereas overall crystallite strain follows a decreasing trend with increasing pO_2. Figure S1c, Supporting Information, shows a gradual decrement in average peak FWHM. So, it is evident that increasing pO_2 improves crystalline quality and nanocrystallite size with additional crystal orientations.

The above growth process of β-$Ga_{2-x}W_xO_3$ NC comes under reactive deposition in an O_2 environment and can be explained through the kinetics of PLD.[40] The lowest pO_2 (5 mTorr) follows "vacuum-like" growth dynamics with almost no interaction between plasma species (ablated from the target after laser incident) and ambient O_2.[40] Next comes the "Transition" regime at 50 mTorr growth pressure with moderate interaction with ambient O_2.[40] 100 mTorr onward is a "diffusion-like" regime, where the ambient O_2 significantly reacts with the incoming plasma plume to facilitate O_2-rich film deposition.[40] The plasma plume, coming from the target, consists of various species, such as atoms, ions, molecules, clusters, electrons, etc. While traveling from the source to substrate, these species react with the ambient gas (O_2 in this case). Additionally, the mean free path (MFP) of

corresponding adatoms differs from each other. The MFP is defined as:

$$\lambda = \frac{K_B \times T}{\sqrt{2} \times P \times \pi \times d_m^2} \quad (4)$$

where K_B is the Boltzmann constant, T is the temperature of the gas, P is the pressure, and d_m is the mean diameter; $d_m = (d_{O_2} + d_{species})/2$. Evidently, the MFP values for Ga and W are different (due to the difference in ionic radius) and reduce gradually with increasing pO_2. The higher pO_2 during the growth process reacts with the plasma species and forms bigger clusters. Also, the ambient pressure controls the phase stabilization after reaching the substrate at an elevated temperature. Various processes on the substrate together control the overall growth dynamics, such as nucleation, interdiffusion, surface diffusion, outdiffusion, etc. The adatoms have higher kinetic energy and outdiffusion probability in a vacuum-like regime. Additionally, the W species possess greater kinetic energy than Ga (due to the difference in ionic mass) and outdiffuse faster. This ends up with W deficit β-$Ga_{2-x}W_xO_3$ thin film on Si substrate at the vacuum-like regime. Photoluminescence (PL) analysis (shown later) supports the exact nature under lower pO_2. This higher W migration affects the crystalline quality and induces low-intensity, broad XRD peaks (Figure 2a and Figure S1c, Supporting Information). Nevertheless, the high-pressure diffusion-like growth dynamics restricts W re-evaporation and improves W incorporation into the β-Ga_2O_3 host. Simultaneously, the surface diffusion rate decreases dramatically with higher O_2 presence and forms larger clusters throughout the growth front. Besides the increasing partial pressure from the vacuum-like to diffusion-like regime, the PLD growth dynamics changes from nanocrystalline to VAN phase. There is no sharp transition point, and the control parameters depend on the source materials and other growth parameters. Nevertheless, researchers have utilized this mechanism to demonstrate multifunctional VAN architectures. Horide et al.[41] indicated VAN-type oxide perovskite heterointerface, under high partial pressure diffusion-like growth region, with precise control over oxide functionality and superconductivity. Whereas Baiutti et al.[31] successfully stabilized high-entropy manganite VAN framework in the vacuum-like arrangement. Recently we have manifested close compact nanocolumnar β-Ga_2O_3 on Si substrate while growing in the transition region.[21] With controlled growth parameters, we exhibited phase pure columnar β-Ga_2O_3 NC with enhanced optical properties. Here, we are controlling the W incorporation by varying pO_2. A schematic in Figure S1d, Supporting Information, illustrates the increasing W content inside primitive β-Ga_2O_3 crystal structure with increasing pO_2.

Figures S2a,b, Supporting Information, show the bare surface elemental mapping (SEM-EDS mapping) of oxygen and gallium in the 5 mTorr sample, respectively, whereas Figures S2c,d, Supporting Information, depict the same for the 150 mTorr sample. It is evident from the maps that, upon tailoring from vacuum-like toward diffusion-like growth mode, Ga gets less dispersed and forms a nanocluster-like distribution, whereas oxygen shows higher atomic concentration. Due to the overlapping of W-Mα and Si-Kα peaks, the SEM-EDS mapping of W is not reliable enough to comment on. The electron probe microanalysis- wavelength dispersive spectrometers (EPMA-WDS) color mapping (**Figure 3**a) of W for the 150 mTorr sample showed the W-rich nanoregions evenly dispersed in W-deficit bulk. Additionally, core-level XPS analysis shows clear evidence of increasing W incorporation with additional pO_2. Cross-sectional transmission electron microscopy (TEM) and corresponding electron diffraction pattern (Figure 3b,c) support polycrystalline nature, and high-angle W-rich vertical nanocolumns along the growth direction. Correlating these findings with the aforementioned structural analysis, it is evident that transition regime onward, the surface diffusion probability of W gets restricted and starts nucleating with host β-Ga_2O_3 in selective nanoregions throughout the growth front. As a result, in nanocolumnar growth mode, there is segregation between W-rich β-$Ga_{2-x}W_xO_3$ nanocolumns within the W-deficit host. The competitive growth dynamics of vertically aligned nanocolumns inside the W-deficit β-$Ga_{2-x}W_xO_3$ shell tailors the crystal orientation significantly. Earlier, we have schematically (Figure 2d) shown how the O_2 partial pressure navigated preferred planes, driven by the asymmetric surface energy distribution and thermal conductivity along different crystal planes. We believe that selective W incorporation under the high-pressure conditions tailors the relative surface energies further and facilitates additional crystal planes ((400), (600), and ($\bar{8}$01)) along β-$Ga_{2-x}W_xO_3$ nanocolumns. A schematic in Figure 3f explains the β-$Ga_{2-x}W_xO_3$ VAN architecture grown on a Si substrate.

For further confirmation of the β-$Ga_{2-x}W_xO_3$ VAN framework, the interface between the Ga-rich oxide matrix and W-rich column was analyzed using atom probe tomography (APT). **Figure 4**a shows the ion map of the Ga-rich and W-rich oxide regions. Additionally, the ion maps portray an isoconcentration surface (decomposed W 50 at% a confidence of $\sigma-3$). The ion map shows that there is a distinct elemental segregation between the regions that are rich in W-rich oxide and Ga-rich oxide, with only a small amount of elemental mixing occurring between the two phases. This is confirmed through the proximity histogram in Figure 4b.

PL spectroscopy reveals the recombination dynamics of photogenerated carriers.[42–45] Depending on the trap-state density and thermodynamically favorable transitions, the PL peak position and spectrum intensity are modulated according to the optimized growth conditions. Such characterization plays an essential role while tailoring and optimizing the material synthesis for photonic and optoelectronic applications. The PL data of GWO NC films are shown in **Figure 5**. In the case of β-Ga_2O_3 and related ternary alloys, the luminescence behavior is well known to the research community.[1,14,18,21] The recombination path is dominated mainly by donor-acceptor pairs, where O_2 vacancies (V_O), interstitial Ga defects (Ga_i), and selective shallow impurities (Si, Sn) act as donor level and Ga vacancies (V_{Ga}), V_O–V_{Ga} complexes, Mg doping, N doping, etc. work as acceptor levels. Also, bound excitonic or self-trap excitonic transitions may be possible owing to its high exciton binding energy. Additionally, selective transition metal doping can potentially manipulate the favorable energy levels between valence and conduction bands.[46] According to the literature, there are three transition bands: UV-blue, green, and yellow-red. Figures 5a,b portray the modulation of the PL peaks with increasing pO_2. Corresponding peak positions are in good agreement with the existing literature. With increasing O_2 pres-

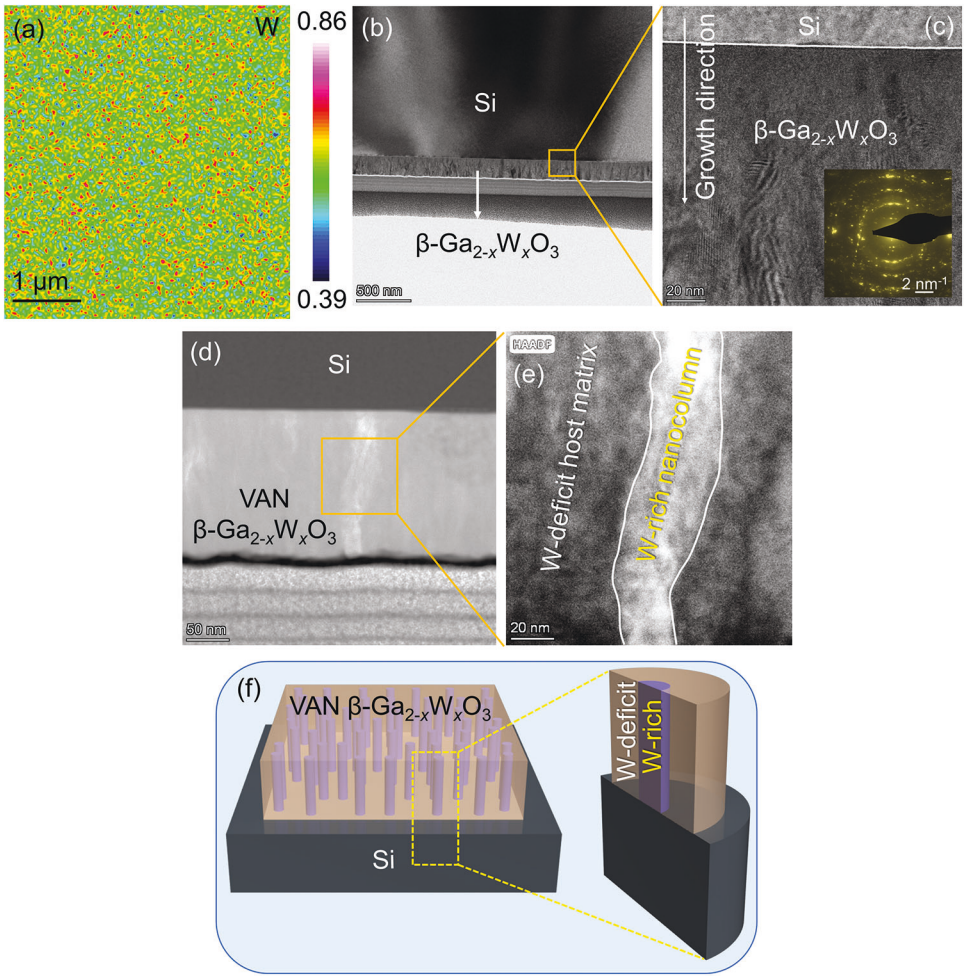

Figure 3. a) Bare surface EPMA-WDS color mapping of W for the 150 mTorr sample; b,c) Low and high-resolution cross-sectional TEM images of the 150 mTorr sample and corresponding electron diffraction pattern; d,e) Low and high-resolution HAADF STEM images of β-$Ga_{2-x}W_xO_3$ VAN heterostructure on a Si platform; f) A schematic of β-$Ga_{2-x}W_xO_3$ VAN heterostructure on a Si substrate.

ence, there is a gradual red shift of the peaks. Initially, the characteristic peaks are in the blue and green band (5 mTorr) and systematically become dominated by the red emission peak (150 mTorr). It is worthwhile to understand the structural and chemical nature of W introduced β-Ga_2O_3 to explain corresponding optical transitions. Tungsten is a transition metal with six possible valence electrons and can serve as a triple electron donor (at the max) per atom while sitting at the Ga site inside β-Ga_2O_3 lattice. So, the recombination probability from the W site is relatively more prominent due to higher free electron density around the W lattice point. Inside β-Ga_2O_3 crystal structure, there are two Ga sites, tetrahedral and octahedral, which can be replaced by foreign metal atoms.[46] W at the tetrahedral Ga site can serve as a shallow donor and it improves n-type conductivity. Such donor states exhibit a UV-blue emission band. Nevertheless, W at the octahedral Ga site facilitates deep-level donor states and enables yellow-red emissions. However, smaller distortion at octahedral sites leads to lower formation energy while incorporating W into β-Ga_2O_3 host matrix. Therefore, the occupancy probability at octahedral sites is higher than at tetrahedral sites, and it leads to favorable transitions from deep-level states near mid-gap energy. With increasing pO_2, the luminescence shows a gradual red shift and increase in peak intensity. Correlating this with structural behavior, it is evident that increasing W incorporation dominates the recombination dynamics as growth moves from vacuum-like to diffusion-like regime. We believe that native DA pairs facilitate blue and green transitions. With W incorporation, the transition probability from deep levels increases and shows high-intensity red-shifted PL spectra. A schematic in Figure 5c explains all possible transitions in the β-$Ga_{2-x}W_xO_3$ NC films. For the highest pO_2, the PL intensity reduced a bit which can be due to structural deformation owing to excessive W incorporation during the growth process. Among all, the pO_2 = 150 mTorr sample shows the highest peak intensity and is thus estimated to have the best device performance.

At this point, it is essential to clarify the transition from β-$Ga_{2-x}W_xO_3$ VAN structure. As we believe, the core with W-rich β-$Ga_{2-x}W_xO_3$ composition facilitates the longer wavelength transition and the host W-deficit β-$Ga_{2-x}W_xO_3$ carries its native DA-assisted blue-green wavelength range. The UV transition might also exist, but below the resolution limit and, thus, it cannot be fitted with the Gaussian assumption. So, it is noticeable from

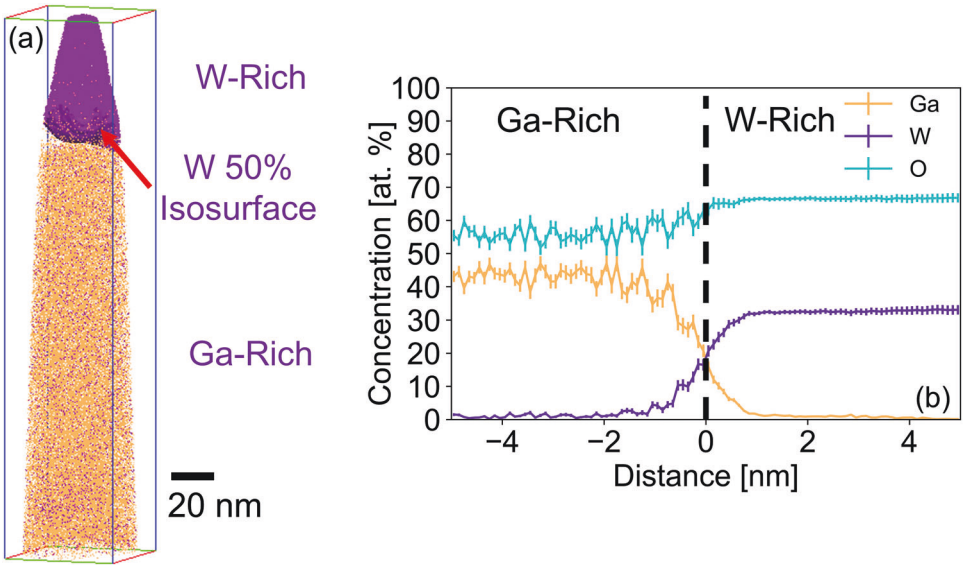

Figure 4. Atom probe tomography of β-$Ga_{2-x}W_xO_3$ VAN heterostructure. a) Ion maps of GaO and WO_2 as well as an isoconcentration surface of decomposed W (50 at% at a σ-3 confidence). b) Proximity histogram in relation to the isoconcentration surface depicting the decomposed Ga, W, and O elemental concentration. The Ga-rich oxide is on the left-hand side of the graph, and the W-rich oxide is on the right-hand side.

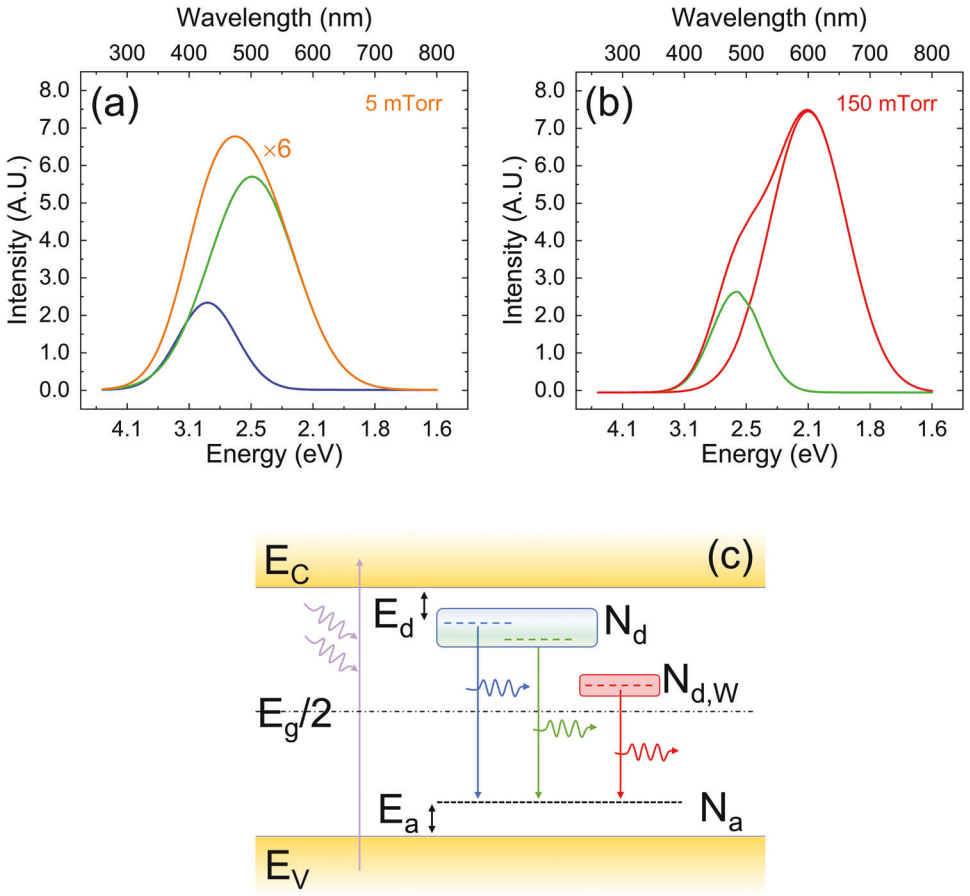

Figure 5. a,b) Room temperature PL spectroscopy with increasing O_2 partial pressure (5 and 150 mTorr), respectively; c) schematic of photogenerated carrier dynamics in β-$Ga_{2-x}W_xO_3$ VAN architecture.

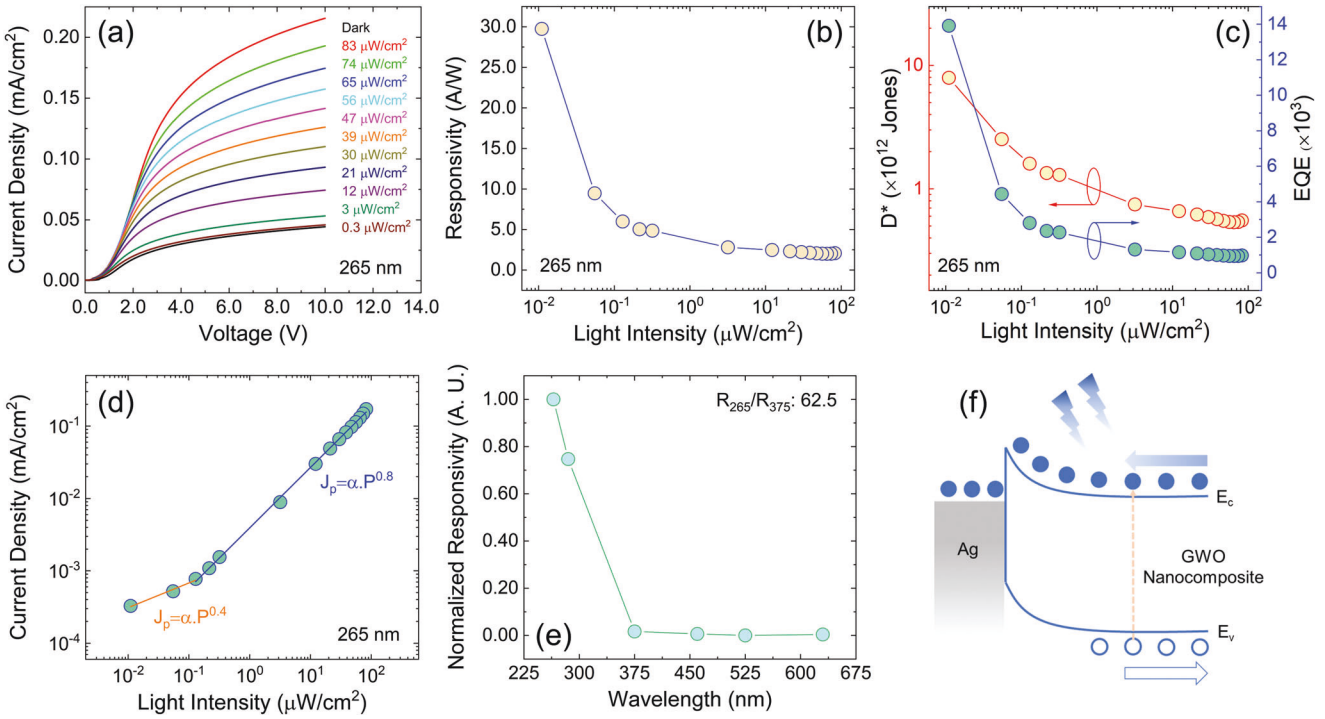

Figure 6. Steady-state device performance: a) dark and photocurrent under forward bias; b) incident power-dependent responsivity at 265 nm irradiation and 10 V forward bias; c) incident power-dependent detectivity and EQE at 265 nm irradiation and 10 V forward bias; d) incident power-dependent photocurrent density at 265 nm irradiation and 10 V forward bias; e) wavelength-dependent normalized responsivity at 10 V forward bias; f) empirical band diagram at the interface of the metal–semiconductor junction.

the aforementioned structural, topographical, chemical, and optical characterizations that the proposed growth policy is facilitating VAN-type architecture with asymmetric donor energy level distribution at the interface between W-rich core and W-deficit shell, thus facilitating interfacial built-in potential. A schematic is shown later, explaining the empirical band at the kink of the asymmetrical W distribution (Figure 8c).

We have fabricated a simple metal-semiconductor-metal (MSM) type UV PD, where β-$Ga_{2-x}W_xO_3$ VAN serves as the active material with a silver top metal contact. The trivial fabrication process and relatively low-cost metal contact have been chosen intentionally to demonstrate a cost-effective approach for UV solar-blind photodetection. Notably, the Ag and β-$Ga_{2-x}W_xO_3$ are forming a Schottky contact, as shown in **Figure 6**f. The carrier exchange mechanism at the metal–semiconductor interface is mainly dominated by thermionic emission, which requires enough energy to cross the typical Schottky junction barrier. Additionally, there is a certain probability of thermionic field emission or field emission-assisted tunneling through the depletion region. The metal–semiconductor interface trap states play an essential role in this tunneling process. As shown earlier, PL characterization confirms the 150 mTorr as the best NC for optoelectronic application with sufficient W incorporation and the lowest possible optical defect density. Assertively, 150 mTorr is the sample for further investigation and shows the lowest dark current (Figure S4b, Supporting Information) and highest responsivity (Figure S4c, Supporting Information) under initial investigation with Ag point contact (Figure S4a, Supporting Information). Therefore, we focussed our further device characterization and discussion on this particular set of samples fabricated under optimum conditions. Figure 6a shows the forward bias I–V characteristics under dark and illumination conditions. As a starter, we used 265 nm photoexcitation with varying power densities. The typical nonlinear behavior of I–V characteristics is due to the back-to-back metal-semiconductor Schottky junction. With increasing incident photon density, it shows gradually increasing photocurrent. For further analysis, we fixed the bias at 10 V and calculated responsivity, detectivity, and external quantum efficiency (EQE) under increasing illumination power density. Responsivity (R), detectivity (D^*) and EQE of a typical PD are defined as the following equations:

$$R_\lambda = \frac{j_{p,\lambda} - j_d}{P_\lambda} \tag{5}$$

$$D^* = \frac{R_\lambda}{\left(2ej_d\right)^{1/2}} \tag{6}$$

$$\mathrm{EQE} = \frac{R_\lambda hc}{e\lambda} \times 100\% \tag{7}$$

where photocurrent density, dark-current density, incident photon power density, charge of an electron, and wavelength are defined as I_p, I_d, P, e, and λ, respectively. Figure 6b shows responsivity at 10 V bias with varying incident photon (265 nm) power density. The highest responsivity value ≈30 A W^{-1} is measured

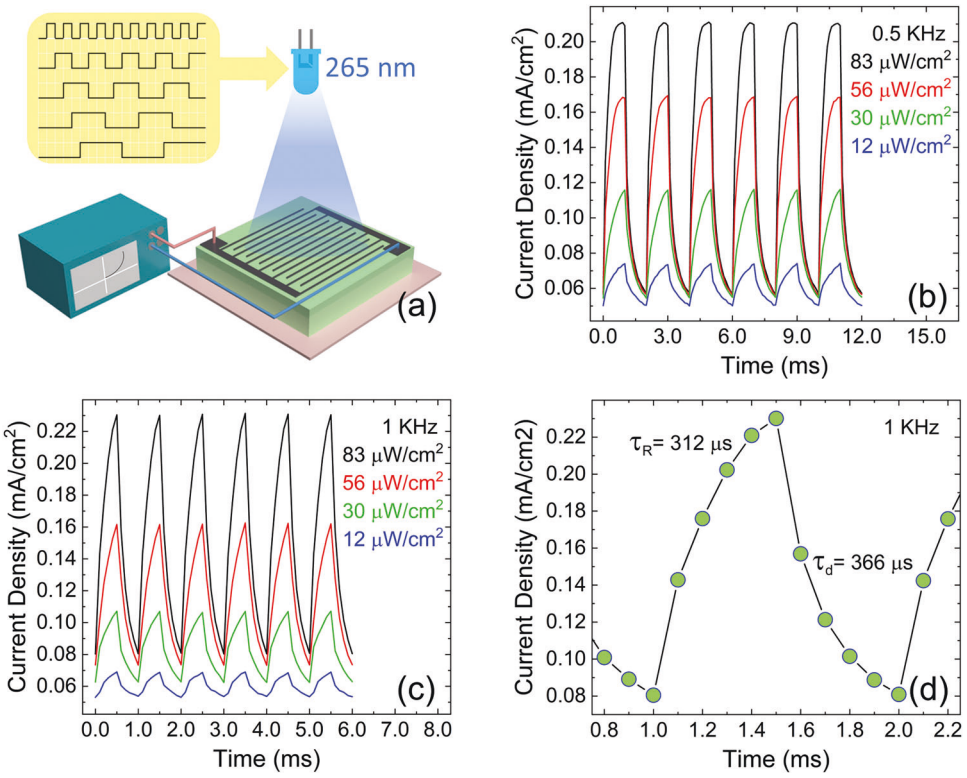

Figure 7. High-frequency transient photo response at 265 nm irradiation and 10 V forward bias: a) schematic of device characterization setup indicating modulation in photoexcitation; b,c) transient switching photo response at 0.5 and 1 kHz under varying photoexcitation power; d) magnified switching photo response at 1 kHz, identifying the rise and fall time of the device.

under 0.01 μW cm^{-2} incident power density. Exponentially decaying responsivity has been observed with increasing photon power density, a signature behavior of MSM-type UV PD. Under intense photon incidents, the excessive photogenerated carriers collide with each other while going toward metal contact and recombining partially without being collected in the external circuit. In short, effective lifetime and drift/diffusion length reduced significantly beyond a critical point. Corresponding D^* and EQE also show similar behavior with an increasing power density (Figure 6c). The highest D^* and EQE values are 7.9 × 10^{12} Jones and 1.4 × 10^4%, respectively. Figure 6d depicts the incident photon power dependent modulation of photocurrent density. The relation can be expressed as $j_p = \alpha.P^{\beta}$, where photocurrent density and incident power are represented as j_p and P. α and β are fitting parameters. $\beta < 1$ is typical for MSM-type device configuration and can be correlated with complex processes inside the material, such as photogeneration, recombination, carrier flow, carrier trapping, etc. The slope reduction at lower incident power reflects the modulation of photogenerated carrier dynamics under weak photoexcitation. For further investigation, we have evaluated responsivity under different wavelength photon illumination. Figure 6e depicts the wavelength-dependent responsivity under a 10 V bias. There is a sharp fall in photoresponse beyond 300 nm, thus acting as solar-blind UV PD with a high rejection ratio of ≈62 (R_{265}/R_{375}).

To demonstrate the potential of this novel approach for future prototyping, it is imperative to comment on the transient device response. Also, it is noteworthy to investigate high-frequency response along with slower switching conditions to visualize frequency-dependent device performance. **Figure 7**a is the schematic of the experimental setup where the fabricated sample is illuminated by the 265 nm LED light with varying power and frequency. Transient photoresponse under 0.5 and 1.0 kHz illumination at 10 V bias is shown in Figure 7b,c. In contrast, low-frequency switching data is shown in Figure S5, Supporting Information. It illustrates a gradually decreasing on/off ratio with lower incident photon power density but an outstanding on/off ratio over a wide frequency range (50 mHz to 5 Hz). Figure 7d shows the effective rise time and decay time calculation under alternative triggering conditions. The optimized β-$Ga_{2-x}W_xO_3$ VAN-based PD shows 312 and 366 μs as rise and decay times, respectively, under high-speed (1 KHz) switching condition. The transient response of the optimized device mentioned here is higher than the top ≈80% of existing reports on NC-based UV PD in the recent literature. We implemented a comparison (**Table 1**) with recent literature along with our findings to evaluate the novelty of the present work.

Figure 8a shows the magnified I–V characteristics under different illumination power densities at 265 nm photoexcitation. A clear shift of V_{oc} and I_{sc} supports the photovoltaic nature, which was predicted earlier, of the fabricated MSM-PD. Increasing incident power density promotes additional photogenerated carriers and shows the ascending nature of V_{oc} and I_{sc}. 83 μW cm^{-2} photoexcitation reflects 19 mV V_{oc} and 55 nA cm^{-2} I_{sc} values. Further, we measured transient device performance in photovoltaic mode

Table 1. Figure of merits of recent NC-based PDs.

SL No.	Device configuration	Spectral range	τ_{rise}/τ_{decay}	Responsivity [A W^{-1}]	Detectivity [Jones]	EQE [%]	Self-biased	Refs.
1	ZnS–rGO NC, MSM	200–290	0.31/0.47	–	–	–	no	[47]
2	TiO_2 NPs/Polymer NC, junction	240–400	0.021/0.023	200	3.7×10^{14}	8.5×10^4	no	[48]
3	ZnO NPs/Polymer NC, junction	320–425	0.003/0.003	2.32	8.45×10^{12}	782	no	[49]
4	ZnO NRs/Cellulose NFs NC, junction	UV	26/26	5.8×10^{-1}	–	–	no	[50]
5	WS_2-QDs/RGO NC, MSM	405	1.5/1.8	5.22×10^{-3}	1.6×10^6	–	no	[51]
6	Cu_2SnS_3 QDs/ZnO NC, junction	UV–vis–NIR	12/6.3	2.8	1.8×10^{12}	9.6	no	[52]
8	Graphdiyne/ZnO NC, MSM	330–375	6.1/2.1	1260	–	4250	no	[37]
9	ZnO NPs/C-TPD NC, junction	UV–vis	–	1.28	6.5×10^{12}	408	yes	[35]
10	NiO_x/PbI_2 NC, junction	UV–vis	$5.8 \times 10^{-8}/1.68 \times 10^{-8}$	0.5	6×10^{12}	70–90	yes	[53]
11	ZnS–polyaniline NC, MSM	UV–vis	0.98/1.27	396 at 86 V	1.68×10^{13}	1.3×10^{-5}	yes	[54]
12	$Ga_{2-x}W_xO_3$ VAN, MSM	265	$3.12 \times 10^{-4}/3.66 \times 10^{-4}$	29.7	7.9×10^{12}	1.4×10^4	yes	This work

(Figure 8b), which shows an excellent on/off ratio under zero bias condition. Although there is no lateral junction formation along the growth direction, this β-$Ga_{2-x}W_xO_3$ VAN-type architecture with asymmetric donor energy level distribution at the interfaces between W-rich core and W-deficit shell facilitates an interfacial built-in potential. These vertical nanoregions with asymmetric Fermi energy distribution promote self-assisted segregation of photogenerated carriers. Figure 8c shows an empirical band diagram explaining the photogenerated carrier flow across the vertical junctions. This novel device architecture with a low-cost facile fabrication technique promotes self-powered UV photodetection in the solar-blind spectrum and has immense potential for further implementation in advanced Si based photonics or optoelectronics.

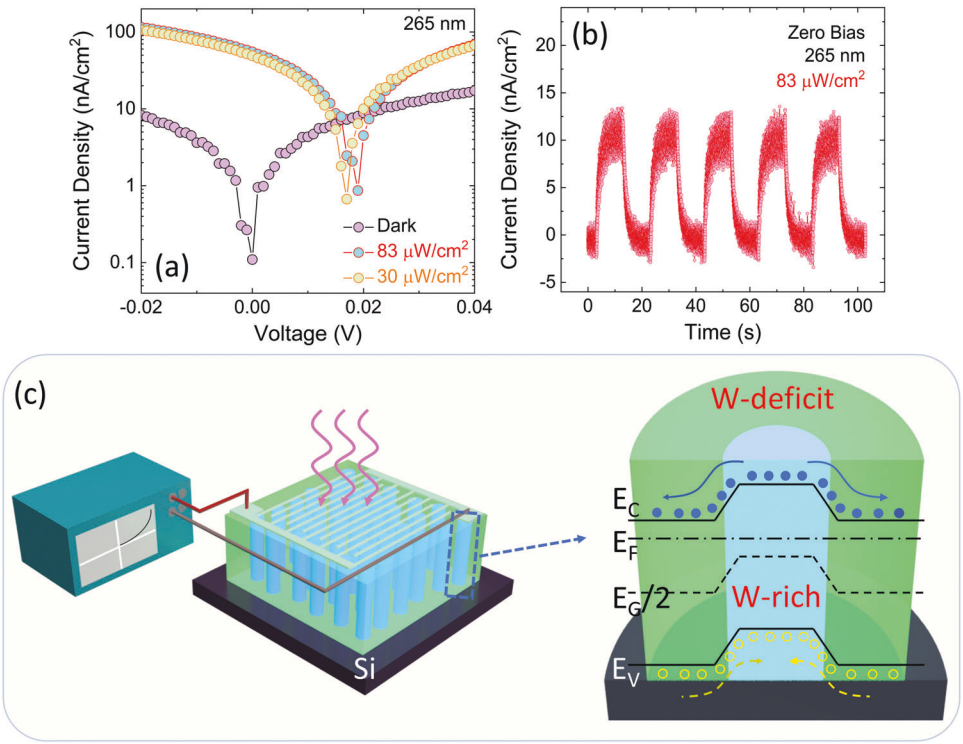

Figure 8. Zero bias device performance under 265 nm illumination: a) dark and photocurrent; b) transient photocurrent for 50 mHz switching frequency and zero bias; c) empirical band diagram at the interface of vertical β-$Ga_{2-x}W_xO_3$ VAN heterostructure, showing the preferred flow of photogenerated carrier under zero bias condition.

3. Conclusions

In summary, we have demonstrated precisely controlled W incorporated β-$Ga_{2-x}W_xO_3$ VAN architecture with asymmetric donor energy distribution between W-rich β-$Ga_{2-x}W_xO_3$ nanocolumns and W-deficit bulk. Structural, morphological and optical characteristics clearly show a progressive transition from nanocrystalline to VAN-type β-$Ga_{2-x}W_xO_3$ framework, while the deposition parameters were tailored from vacuum-like toward diffusion-like growth mode. The MSM-type device with Ag interdigital electrode demonstrates a low-cost, simple device platform to provide solar-blind UV photodetection on Si platform. Overall, device performance is inspiring and is comparable with the top 20% of the reports on NC-based deep-UV photodetectors. This pioneering effort to facilitate VAN-based functional architecture promotes the self-powered operating configuration and can be exploited further for advanced deep UV optoelectronic and photonic applications.

4. Experimental Section

Materials and Target Synthesis: Tungsten-incorporated gallium oxide PLD targets were produced from the conventional solid-sate reaction method. High purity β-Ga_2O_3 (99.999%) and WO_3 (99.999%) powder precursors procured from Sigma Aldrich were weighed in stoichiometric proportions according to the chemical formula $Ga_{2-x}W_xO_3$ where $x = 0.1$. The concentration of W was restricted with desirable concentration to avoid multiphase formation, which could drastically reduce the optical band gap[20] or facilitate a dual band of optical absorption. The powders were pulverized in an agate mortar under a volatile liquid environment with the aid of acetone to decrease the particle size and ensure homogeneity. Then, the homogenous mixture was calcined at 1100 °C for 12 h with a heating and cooling ramp rate of 5°C min^{-1} in a SentroTech muffle furnace. The calcinated powder was mixed thoroughly with polyvinyl alcohol (PVA) binder. The later mixture was then pressed using a uniaxial hydraulic press with an applied load of 1.5 ton for 3 min to create the circular pellet with dimensions of 25.4 mm diameter and 5 mm thickness. The pellet was then subjected to sintering after binder burnout, where the temperature was invariable at 100 °C for 60 min. During the sintering process, the pellet was heated to 1350 °C for 12 h using a heating and cooling ramp rate of 5 °C min^{-1}.

Nanocomposite Fabrication: The tungsten incorporated β-Ga_2O_3 thin films were deposited onto Si(100) by the PLD technique, using a KrF excimer laser (λ = 248 nm) with a pulse energy of 220 mJ. The target-substrate distance was set at 45 mm. The substrate temperature and pulsed laser frequency were fixed at 700 °C and 3 Hz, respectively. The O_2 partial pressure varied between the range of 5–200 mTorr.

Material Characterization: Crystal structure and phase identification were studied using XRD; Bruker D8 Discover employing Cu Kα (λ = 1.5406 Å) radiation. The θ–2θ measurements were taken in the range of 15°–61.2° with a step of 0.02°. The X'pert Highscore software was used for profile fitting and phase identification of the XRD pattern.

An FEI SCIOS FIB/SEM dual beam setup was used for TEM sample preparation. The TEM imaging was done in Thermo Scientific Titan Themis probe Cs corrected TEM, equipped with SuperX EDS spectrometer, and was operated at 200 keV. HAADF-STEM was employed to understand the growth of VAN architecture.

W-Mα and Si-Kα line X-ray peaks overlapped with each other. It was challenging to detect W content using the conventional SEM-based EDS method. EPMA, equipped with WDS, was used to analyze the top surface elemental mapping. A distinguished W peak was observed using LIF crystal detector.

Needle samples for APT were fabricated by the standard lift-out and annular milling process using a Thermo Fisher Scientific Hydra Xe-based plasma-focused ion beam.[55] The Supporting Information image (Figure S3, Supporting Information) shows the different stages of APT sample preparation. The APT analysis was conducted in a laser-assisted mode in a LEAP 4000 XR (Cameca). The temperature of the sample was maintained at 40 K. The laser wavelength used was λ = 355 nm. The laser pulse frequency was 100 kHz, and the detection rate (events per pulse) was 0.005 atoms per pulse.[56] Raw atom probe data were reconstructed and analyzed using the Integrated Visualization and Analysis Software, version 3.8.10 (IVAS, Cameca). Isoconcentration surface selection was based on the concentration inflection point measured via a proximity histogram between the decomposed W-deficient and W-rich regions.[57,58] Voxel size was (1.0, 1.0, 1.0) nm and the delocalization was (3.0, 3.0, 1.5) nm. Bin size was 0.1 nm, and edge polygons were excluded.

Optical and Photodetector Characterization: Excitation for the PL measurements came from a Ti: sapphire laser operating at 80 MHz. Laser pulses of 100 fs duration and 245 nm wavelength were focused on the sample, and the incident power density was 5.5 kW cm^{-2}. A monochromator with a resolution of 0.02 nm, and a photomultiplier tube were utilized for the detection.

After detailed material characterization, the selected optimized samples were loaded in PVD chamber with a metal show mask in front. 100 nm thick Ag was deposited on top, followed by preoptimized contact annealing. A simple MSM configuration was used for the device characterization. Also, the contact surface area was kept the same for both electrodes to minimize the effect of asymmetric depletion region width. Dark and photo *I–V* were measured using Keysight B1500A semiconductor device analyzer. LEDs with varying wavelengths (265, 285, 375, 460, 525, and 630 nm) had been used to investigate the photoresponse of the fabricated devices.

Supporting Information

Supporting Information is available from the Wiley Online Library or from the author.

Acknowledgements

D.D. and F.S. contributed equally to this work. This material is also based upon work supported by the Air Force Office of Scientific Research under award number FA9550-18-1-0387. However, any opinions, finding, and conclusions or recommendations expressed in this contribution are those of the author(s) and do not necessarily reflect the views of the United States Air Force. The authors also acknowledge, with pleasure, support from the National Science Foundation (NSF) with NSF-PREM grant #DMR-1827745. A portion of this research (Chemical Composition Analyses using X-ray Photoelectron Spectroscopy and Atom Probe Tomography) was performed on a project award (10.46936/cpcy.proj.2021.60259/60008213) from the Environmental Molecular Sciences Laboratory, a DOE Office of Science User Facility sponsored by the Biological and Environmental Research program under Contract No. DE-AC05-76RL01830 and also funded in part by a grant from the Washington State Department of Commerce's Clean Energy Fund.

Conflict of Interest

The authors declare no conflict of interest.

Data Availability Statement

The data that support the findings of this study are available from the corresponding author upon reasonable request.

Keywords

β-$Ga_{2-x}W_xO_3$ nanocomposites, pulsed laser deposition, self-biased UV detectors, solar-blind photodetectors, vertically aligned nanocomposites

Received: January 4, 2023
Revised: March 9, 2023
Published online:

[1] X. Hou, X. Zhao, Y. Zhang, Z. Zhang, Y. Liu, Y. Qin, P. Tan, C. Chen, S. Yu, M. Ding, G. Xu, Q. Hu, S. Long, *Adv. Mater.* **2022**, *34*, 2106923.
[2] T. Wang, H. Liang, Z. Han, Y. Sui, Z. Mei, *Adv. Mater. Technol.* **2021**, *6*, 2000945.
[3] Q. Cai, H. You, H. Guo, J. Wang, B. Liu, Z. Xie, D. Chen, H. Lu, Y. Zheng, R. Zhang, *Light Sci Appl* **2021**, *10*, 94.
[4] Y. Zheng, M. N. Hasan, J.-H. Seo, *Adv. Mater. Technol.* **2021**, *6*, 2100254.
[5] A. Mukherjee, V. Ottapilakkal, S. Sagar, B. C. Das, *ACS Appl. Nano Mater.* **2021**, *4*, 8050.
[6] B. H. Le, S. Zhao, X. Liu, S. Y. Woo, G. A. Botton, Z. Mi, *Adv. Mater.* **2016**, *28*, 8446.
[7] C. V. Ramana, R. S. Vemuri, V. V. Kaichev, V. A. Kochubey, A. A. Saraev, V. V. Atuchin, *ACS Appl. Mater. Interfaces* **2011**, *3*, 4370.
[8] L. Ma, Z. Xia, V. Atuchin, M. Molokeev, S. Auluck, A. H. Reshak, Q. Liu, *Phys. Chem. Chem. Phys.* **2015**, *17*, 31188.
[9] V. V. Atuchin, M. S. Lebedev, I. V. Korolkov, V. N. Kruchinin, E. A. Maksimovskii, S. V. Trubin, *J Mater Sci* **2019**, *30*, 812.
[10] P. G. Nalam, D. Das, S. Tan, C. V. Ramana, *ACS Appl. Electron. Mater.* **2022**, *4*, 3115.
[11] D. Das, A. Aiello, W. Guo, P. Bhattacharya, *IEEE Trans. Nanotechnol.* **2020**, *19*, 571.
[12] A. Aiello, D. Das, P. Bhattacharya, *ACS Appl. Nano Mater.* **2021**, *4*, 1825.
[13] D. N. Nath, Z. C. Yang, C. Y. Lee, P. S. Park, Y. R. Wu, S. Rajan, *Appl. Phys. Lett.* **2013**, *103*, 022102.
[14] D. Das, F. S. Escobar, P. G. Nalam, P. Bhattacharya, C. V. Ramana, *J. Lumin.* **2022**, *248*, 118960.
[15] M.-H. Lee, T.-S. Chou, S. Bin Anooz, Z. Galazka, A. Popp, R. L. Peterson, *ACS Nano* **2022**, *16*, 11988.
[16] A. K. Rajapitamahuni, A. K. Manjeshwar, A. Kumar, A. Datta, P. Ranga, L. R. Thoutam, S. Krishnamoorthy, U. Singisetti, B. Jalan, *ACS Nano* **2022**, *16*, 8812.
[17] G. Gutierrez, E. M. Sundin, P. G. Nalam, V. Zade, R. Romero, A. N. Nair, S. Sreenivasan, D. Das, C. Li, C. V. Ramana, *J. Phys. Chem. C* **2021**, *125*, 20468.
[18] S. J. Pearton, J. Yang, P. H. Cary, F. Ren, J. Kim, M. J. Tadjer, M. A. Mastro, *Appl. Phys. Rev.* **2018**, *5*, 011301.
[19] N. Alfaraj, K.-H. Li, M. Alawein, C. H. Kang, L. Braic, N. C. Zoita, A. E. Kiss, T. K. Ng, B. S. Ooi, *Adv. Mater. Technol.* **2021**, *6*, 2100142.
[20] E. J. Rubio, C. V. Ramana, *Appl. Phys. Lett.* **2013**, *102*, 191913.
[21] N. Makeswaran, D. Das, V. Zade, P. Gaurav, V. Shutthanandan, S. Tan, C. V. Ramana, *ACS Appl. Nano Mater.* **2021**, *4*, 3331.
[22] A. N. Nair, M. F. Sanad, R. Jayan, G. Gutierrez, Y. Ge, M. M. Islam, J. A. Hernandez-Viezcas, V. Zade, S. Tripathi, V. Shutthanandan, C. V. Ramana, S. T. Sreenivasan, *Small* **2022**, *18*, 2202648.
[23] S. Misra, H. Wang, *Mater. Horiz.* **2021**, *8*, 869.
[24] H. K. Choi, N. M. Aimon, D. H. Kim, X. Y. Sun, J. Gwyther, I. Manners, C. A. Ross, *ACS Nano* **2014**, *8*, 9248.
[25] V. V. Atuchin, E. N. Galashov, A. S. Kozhukhov, L. D. Pokrovsky, V. N. Shlegel, *J. Cryst. Growth* **2011**, *318*, 1147.
[26] K. A. Kokh, V. V. Atuchin, T. A. Gavrilova, A. Kozhukhov, E. A. Maximovskiy, L. D. Pokrovsky, A. R. Tsygankova, A. I. Saprykin, *J. Microsc.* **2014**, *256*, 208.
[27] V. Garg, B. S. Sengar, V. Awasthi, A. Kumar, R. Singh, S. Kumar, C. Mukherjee, V. V. Atuchin, S. Mukherjee, *ACS Appl. Mater. Interfaces* **2018**, *10*, 5464.
[28] V. Garg, B. S. Sengar, G. Siddharth, S. Kumar, V. V. Atuchin, S. Mukherjee, *Surf. Interfaces* **2021**, *25*, 101146.
[29] C. Patel, R. Singh, M. Dubey, S. K. Pandey, S. N. Upadhyay, V. Kumar, S. Sriram, M. Than Htay, S. Pakhira, V. V. Atuchin, S. Mukherjee, *ACS Appl. Nano Mater.* **2022**, *5*, 9415.
[30] Y. Li, Z. Wang, J. Yao, T. Yang, Z. Wang, J.-M. Hu, C. Chen, R. Sun, Z. Tian, J. Li, L.-Q. Chen, D. Viehland, *Nat. Commun.* **2015**, *6*, 6680.
[31] F. Baiutti, F. Chiabrera, M. Acosta, D. Diercks, D. Parfitt, J. Santiso, X. Wang, A. Cavallaro, A. Morata, H. Wang, A. Chroneos, J. MacManus-Driscoll, A. Tarancon, *Nat. Commun.* **2021**, *12*, 2660.
[32] O. J. Lee, S. Misra, H. Wang, J. L. MacManus-Driscoll, *APL Mater.* **2021**, *9*, 030904.
[33] K.-H. Ha, W. Zhang, H. Jang, S. Kang, L. Wang, P. Tan, H. Hwang, N. Lu, *Adv. Mater.* **2021**, *33*, 2103320.
[34] F. Guo, B. Yang, Y. Yuan, Z. Xiao, Q. Dong, Y. Bi, J. Huang, *Nat. Nanotechnol.* **2012**, *7*, 798.
[35] Y. Fang, F. Guo, Z. Xiao, J. Huang, *Adv. Opt. Mater.* **2014**, *2*, 348.
[36] X. Zhang, E. Zheng, M. R. Esopi, C. Cai, Q. Yu, *ACS Appl. Mater. Interfaces* **2018**, *10*, 24064.
[37] Z. Jin, Q. Zhou, Y. Chen, P. Mao, H. Li, H. Liu, J. Wang, Y. Li, *Adv. Mater.* **2016**, *28*, 3697.
[38] Y.-L. Huang, H.-J. Liu, C.-H. Ma, P. Yu, Y.-H. Chu, J.-C. Yang, *China J. Phys.* **2019**, *60*, 481.
[39] J. Åhman, G. Svensson, J. Albertsson, *Acta Crystallogr C* **1996**, *52*, 1336.
[40] A. Ojeda-G-P, M. Döbeli, T. Lippert, *Adv. Mater. Interfaces* **2018**, *5*, 1701062.
[41] T. Horide, F. Kametani, S. Yoshioka, T. Kitamura, K. Matsumoto, *ACS Nano* **2017**, *11*, 1780.
[42] V. V. Atuchin, V. G. Kesler, V. V. Ursaki, V. E. Tezlevan, *Solid State Commun.*. **2006**, *138*, 250.
[43] M. O. Petrushkov, D. S. Abramkin, E. A. Emelyanov, M. A. Putyato, O. S. Komkov, D. D. Firsov, A. V. Vasev, M. Y. Yesin, A. K. Bakarov, I. D. Loshkarev, A. K. Gutakovskii, V. V. Atuchin, V. V. Preobrazhenskii, *Nanomaterials* **2022**, *12*, 4449.
[44] D. Panda, M. Ranjan Mantri, R. Kumar, D. Das, R. Saha, S. Chakrabarti, *Appl. Surf. Sci.* **2023**, *607*, 154948.
[45] D. Das, D. P. Panda, B. Tongbram, J. Saha, V. Deviprasad, H. Rawool, S. M. Singh, V. Chavan, S. Chakrabarti, *Sol. Energy Mater. Sol. Cells* **2018**, *185*, 549.
[46] H. Peelaers, C. G. Van de Walle, *Phys. Rev. B* **2016**, *94*, 195203.
[47] M. Hajimazdarani, N. Naderi, B. Yarmand, A. Kolahi, P. Sangpour, *Ceram. Int.* **2018**, *44*, 17878.
[48] D. Shao, M. Yu, H. Sun, G. Xin, J. Lian, S. Sawyer, *ACS Appl. Mater. Interfaces* **2014**, *6*, 14690.
[49] E. Zheng, X. Zhang, M. R. Esopi, C. Cai, B. Zhou, Y.-Y. Lin, Q. Yu, *ACS Appl. Mater. Interfaces* **2018**, *10*, 41552.
[50] T. Park, N. Kim, D. Kim, S.-W. Kim, Y. Oh, J.-K. Yoo, J. You, M.-K. Um, *ACS Appl. Mater. Interfaces* **2019**, *11*, 48239.
[51] Abid, P. Sehrawat, C. M. Julien, S. S. Islam, *ACS Appl. Mater. Interfaces* **2020**, *12*, 39730.
[52] S. M. Yadav, A. K. Chaurasia, G. Rawat, A. Pandey, *ACS Appl. Electron. Mater.* **2021**, *3*, 4018.
[53] H. L. Zhu, J. Cheng, D. Zhang, C. Liang, C. J. Reckmeier, H. Huang, A. L. Rogach, W. C. H. Choy, *ACS Nano* **2016**, *10*, 6808.
[54] A. Verma, P. Chaudhary, A. Singh, R. K. Tripathi, B. C. Yadav, *ACS Appl. Nano Mater.* **2022**, *5*, 4860.
[55] A. Devaraj, D. E. Perea, J. Liu, L. M. Gordon, T. J. Prosa, P. Parikh, D. R. Diercks, S. Meher, R. P. Kolli, Y. S. Meng, S. Thevuthasan, *Int. Mater. Rev.* **2018**, *63*, 68.
[56] S. Manandhar, A. K. Battu, A. Devaraj, V. Shutthanandan, S. Thevuthasan, C. V. Ramana, *Sci. Rep.* **2020**, *10*, 178.
[57] D. J. Barton, B. C. Hornbuckle, K. A. Darling, G. B. Thompson, *Microsc. Microanal.* **2019**, *25*, 401.
[58] B. C. Hornbuckle, M. Kapoor, G. B. Thompson, *Ultramicroscopy* **2015**, *159*, 346.